AD-A138 491 CHARACTERIZATION AND SCATTERING OF BOUNDED ULTRASONIC BEAMS(U) GEORGETOWN UNIV WASHINGTON DC DEPT OF PHYSICS T D NGOC ET AL. 16 FEB 84 GUUS-02847 N00014-78-C-0584 1/1

UNCLASSIFIED F/G 20/1 NL

END

DATE FILMED

3-84

DTIC

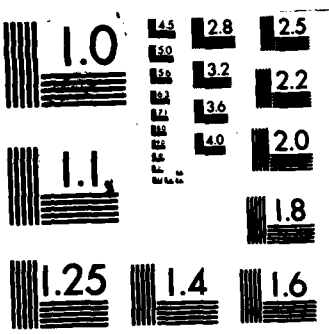

Office of Naval Research

Contract N00014-78-C-0584

Technical Report No. 7

CHARACTERIZATION AND SCATTERING OF BOUNDED ULTRASONIC BEAMS

by

T. D. K. Ngoc, W. G. Mayer, T. H. Neighbors, III

Walter G. Mayer
Principal Investigator
Department of Physics
Georgetown University
Washington, DC 20057

February 1984

Unclassified
SECURITY CLASSIFICATION OF THIS PAGE (When Data Entered)

REPORT DOCUMENTATION PAGE

READ INSTRUCTIONS BEFORE COMPLETING FORM

1. REPORT NUMBER: GUUS-02847	2. GOVT ACCESSION NO. [redacted] 3. RECIPIENT'S CATALOG NUMBER: AD-A138 491
4. TITLE (and Subtitle): Characterization and Scattering of Bounded Ultrasonic Beams	5. TYPE OF REPORT & PERIOD COVERED: Technical, 1 June 83 - 31 Jan. 84
	6. PERFORMING ORG. REPORT NUMBER: TR 7
7. AUTHOR(s): T.D.K. Ngoc, W.G. Mayer, T.H. Neighbors III	8. CONTRACT OR GRANT NUMBER(s): N00014-78-C-0584
9. PERFORMING ORGANIZATION NAME AND ADDRESS: Physics Department, Georgetown University, Washington, DC 20057	10. PROGRAM ELEMENT, PROJECT, TASK AREA & WORK UNIT NUMBERS: 121108
11. CONTROLLING OFFICE NAME AND ADDRESS: Office of Naval Research, Code 412, Arlington, VA 22217	12. REPORT DATE: 16 February 1984
	13. NUMBER OF PAGES: 16
14. MONITORING AGENCY NAME & ADDRESS(if different from Controlling Office)	15. SECURITY CLASS. (of this report): Unclassified
	15a. DECLASSIFICATION/DOWNGRADING SCHEDULE

16. DISTRIBUTION STATEMENT (of this Report)

Approved for public release; distribution unlimited

17. DISTRIBUTION STATEMENT (of the abstract entered in Block 20, if different from Report)

Approved for public release; distribution unlimited

18. SUPPLEMENTARY NOTES

19. KEY WORDS (Continue on reverse side if necessary and identify by block number)

ultrasonics, bounded beam, ultrasonic pulses, acousto-optics, backscattering, reflection at the Rayleigh angle.

20. ABSTRACT (Continue on reverse side if necessary and identify by block number)

An acousto-optic method is indicated with which to analyze the shape of an ultrasonic pulse. A mathematical model is given which describes a non-Gaussian bounded ultrasonic beam. Existing reflection formulations are used to predict the existence of backscattering at flat boundaries at the Rayleigh angle.

DD FORM 1 JAN 73 1473 EDITION OF 1 NOV 65 IS OBSOLETE
S/N 0102-014-6601

Unclassified
SECURITY CLASSIFICATION OF THIS PAGE (When Data Entered)

This Technical Report consists of reprints of papers which have appeared since July 1983, sponsored through Office of Naval Research Contract N00014-78-C-0584. The papers deal with some aspects of ultrasonic beam properties, their mathematical representation, and theoretical predictions related to reflection and scattering.

The first paper deals with an acousto-optic method by which the frequency contents of a pulsed ultrasonic signal can be determined without the introduction of a transducer probe whose presence in the path of the signal might alter the composition or shape of the pulse.

The second paper is concerned with reflection of an ultrasonic signal at a boundary, particularly with the recently mentioned possibilities of the existence of backscattering.

The third article deals with a method of describing methematically a bounded beam which is known not to have a Gaussian cross section, and with the reflected profile of such a non-Gaussian beam.

Walter G. Mayer
Principal Investigator

Washington, February 1984

A-1

Asymmetric light diffraction by pulsed ultrasonic waves

Thomas H. Neighbors, III
The BDM Corporation, 7915 Jones Branch Drive, McLean, Virginia 22102

Walter G. Mayer
Physics Department, Georgetown University, Washington, DC 20057

(Received 29 October 1982; accepted for publication 17 March 1983)

Low-MHz, continuous ultrasonic waves traveling in a transparent medium cause light to be diffracted into discrete diffraction orders when light and sound propagation directions are normal to each other. When pulsed ultrasonic waves are used the diffraction orders split into secondary orders which are asymmetric with respect to the central diffraction order. This splitting is derived and a general expression provided for the intensity as a function of the ultrasonic pulse Fourier spectra. Examples are provided which demonstrate the degree of asymmetry for an exponential driving pulse and the convergence to the classic Raman–Nath results when the pulse approaches a continuous wave.

PACS numbers: 43.35.Sx, 43.20.Bi

INTRODUCTION

Optical probing of ultrasonic waves had its origins in 1932 through the independent observations by Debye and Sears[1] in Washington and Lucas and Biquard[2] in Paris that an ultrasonic beam in a liquid acts like a diffraction grating when illuminated by normally incident light. In 1935 Raman and Nath[3–5] explained these observations by treating the ultrasonic beam as a moving phase grating. Their theory successfully predicted the diffracted light angular distribution and the relative intensities in the diffraction orders as a function of sound intensity, optical and ultrasonic wavelengths, and ultrasonic beam thickness.

Refinements of the Raman–Nath theory have been used to investigate a broad spectrum of theoretical and experimental conditions related to light diffraction by ultrasound. This has ranged from the theoretical investigation of light diffraction by superposed ultrasound by Murty[6] to the use of optical probing for the investigation of the growth of higher harmonics in finite amplitude progressive waves by Zankel and Hiedemann[7] and Breazeale and Hiedemann.[8] Hargrove[9] extended the Raman–Nath theory to include the prediction of the diffraction pattern for arbitrary ultrasonic waves as illuminated by Gaussian light beams. Zitter[10] in turn applied this extended theory to light diffraction by symmetric short ultrasonic pulses. Other extensions have included the examination of light modulation by ultrasonic waves in the presence of amplitude optical gratings by Calligari *et al.*[11–13]

Our current interest is prompted by the recent experimental work of Häusler *et al.*,[14] which demonstrated the production of structured diffraction patterns by pulsed ultrasonic waves and provided qualitative verification of the pulsed diffraction theory presented by Zitter.[10] This paper expands the examination of Raman–Nath diffraction by pulsed ultrasonic waves to include nonsymmetric pulses which are composed of modulated sinusoidal waves of wavelength λ_0 with a pulse repetition interval λ_p.

There are three primary results. First, for small values of the pulse Raman–Nath parameter, optical probing provides a direct technique for the relative measurement of the ultrasonic pulse amplitude spectra. Second, the splitting of the intensities in the first Raman–Nath diffraction order into satellite orders as discussed by Zitter[10] also occurs for the central, second, third, etc., diffraction orders. A general expression is provided for the calculation of these intensities. Third, the intensity distribution within the diffraction orders is asymmetric, i.e., the intensity in the positive mth diffraction is not equal to the intensity in the negative mth order.

I. GENERAL THEORY

When a monochromatic light beam of frequency f, wavelength λ, and width $2l$, is normally incident on an ultrasonic beam of diameter D, frequency f_0, and wavelength λ_0, the amplitude distribution of the light in the farfield is given by the diffraction integral as

$$A(\theta,t) = Ce^{i\omega t}\int_{-l}^{l} e^{ikx\sin\theta}e^{iv(\alpha)}dx\,, \tag{1}$$

where

C = the normalization constant

$\omega = 2\pi f$

$k = 2\pi/\lambda$

θ = the farfield angle

t = time

$\omega_0 = 2\pi f_0$

$k_0 = 2\pi/\lambda_0$

$\alpha = \omega_0 t - k_0 x\,,$

with $v(\alpha)$ representing the phase change in the light wave front due to the ultrasonic wave. For a continuous wave excitation

$$v(\alpha) = \nu\sin(\alpha)\,, \tag{2}$$

with

$$\nu = 2\pi\mu D/\lambda \tag{3}$$

defined as the Raman–Nath parameter where μ is the maxi-

 0001-4966/83/070146-07$00.80

mum variation of the media refractive index. For an arbitrary pulsed ultrasonic wave with functional form $f(x,t,t_p)$ where t_p is the pulse repetition period, v can be expressed in terms of the Fourier expansion of $f(x,t,t_p)$ as

$$v(\alpha_p) = \sum_{n=0}^{\infty} \nu_n \sin(n\alpha_p + \phi_n), \tag{4}$$

with

$$\omega_p = 2\pi/t_p$$
$$\alpha_p = \omega_p t - k_p x$$
$$\nu_n = a_n \nu$$
$$k_p = \omega_p / v$$
$$v = \text{ultrasonic velocity},$$

where a_n and ϕ_n are the amplitude and phase of the nth Fourier component of the pulse. In this case μ is determined by the pulse peak amplitude.

Substituting Eq. (4) into Eq. (1) and moving the dc component of $v(\alpha_p)$ outside of the integral yields:

$$A(\theta,t) = Ce^{i\omega t} e^{i\nu_0 \sin\phi_0} \int_{-l}^{l} e^{ikx\sin\theta} \times \prod_{n=1}^{\infty} e^{i\nu_n \sin(n\alpha_p + \phi_n)}\, dx. \tag{5}$$

Using the identity[10]

$$e^{i\epsilon\sin\beta} = \sum_{r=-\infty}^{\infty} J_r(\epsilon) e^{ir\beta}, \tag{6}$$

the product expression in Eq. (5) can be rewritten as

$$\prod_{n=1}^{\infty} \{\ \} = \sum_{m=-\infty}^{\infty} \Psi_m e^{im\alpha_p}, \tag{7}$$

where $J_r(\epsilon)$ is the rth order Bessel function and

$$\Psi_m = \sum_{r_2=-\infty}^{\infty} \cdots \sum_{r_n=-\infty}^{\infty} J_{r_1(m)}(\nu_1)\cdots J_{r_n}(\nu_n)\cdots \times \exp\{i[r_1(m)\phi_1 + \cdots + r_n\phi_n + \cdots]\}, \tag{8}$$

with $r_1(m) = m - 2r_2 - \cdots - nr_n - \cdots$. Substituting Eq. (7) into Eq. (5) and performing the integration yields:

$$A(\theta,t) = \frac{Cl}{2} \sum_{m=-\infty}^{\infty} \left(\Psi_m e^{i[(\omega + m\omega_p)t + \Delta_0]} \frac{\sin\Omega_m}{\Omega_m} \right), \tag{9}$$

with $\Delta_0 = \nu_0 \sin\phi_0$ and

$$\Omega_m = (k\sin\theta - mk_p)l. \tag{10}$$

Since the Ψ_m terms are complex, Eq. (9) can be rewritten as

$$A(\theta,t) = \frac{Cl}{2} \sum_{m=-\infty}^{\infty} (\{\Psi_m^{\mathrm{Re}} \cos[(\omega + m\omega_p)t + \Delta_0] - \Psi_m^{\mathrm{Im}} \sin[(\omega + m\omega_p)t + \Delta_0]\} + i\{\Psi_m^{\mathrm{Re}} \sin[(\omega + m\omega_p)t + \Delta_0] + \Psi_m^{\mathrm{Im}} \cos[(\omega + m\omega_p)t + \Delta_0]\}) \frac{\sin\Omega_m}{\Omega_m}, \tag{11}$$

where Re and Im denote the real and imaginary components of Ψ_m. The light intensity is then given by the square of the real part of Eq. (11).

$$I(\theta,t) = \{\mathrm{Re}\, A(\theta,t)\}^2. \tag{12}$$

To obtain the measured response of a fast photodetector it is necessary to take the time average intensity over an interval τ which is long compared to the period of the incident light and at the same time is short compared to the pulse repetition rate, i.e.,

$$\bar{I}(\theta,t_0) = \frac{1}{\tau} \int_{t_0}^{t_0+\tau} I(\theta,t)\, dt, \quad \omega \gg \frac{2\pi}{\tau} \gg \omega_p. \tag{13}$$

Normalizing Eq. (13) to the peak light intensity in the absence of an ultrasonic wave, i.e., $\theta = 0$, $\nu_m = 0$ for $m > 0$, yields

$$\bar{I}(\theta,t_0) = \sum_{m=-\infty}^{\infty} \sum_{n=-\infty}^{\infty} \frac{\sin\Omega_m}{\Omega_m} \frac{\sin\Omega_n}{\Omega_n} \times \{\{\Psi_m^{\mathrm{Re}}\Psi_n^{\mathrm{Re}} + \Psi_m^{\mathrm{Im}}\Psi_n^{\mathrm{Im}}\}\cos(m-n)\omega_p t_0 - \{\Psi_m^{\mathrm{Im}}\Psi_n^{\mathrm{Re}} - \Psi_m^{\mathrm{Re}}\Psi_n^{\mathrm{Im}}\}\sin(m-n)\omega_p t_0\}, \tag{14}$$

which is independent of ν_0. The same results could have been obtained by incorporating ν_0 into the unperturbed media index of refraction. Due to the $\sin x/x$ term in Eq. (14) the light intensity will exhibit maxima when $\Omega_m = 0$, i.e., at the angles θ_m which satisfy the relationship

$$\sin\theta_m = \pm m(\lambda/\lambda_p). \tag{15}$$

Equation (15) is the same as the result obtained in continuous wave diffraction theory[3] except that the diffraction angle is determined by the ratio of the incident light wavelength to the pulse spatial duration. Setting $n = m - 1$ and evaluating the product $(\sin\Omega_m/\Omega_m)(\sin\Omega_n/\Omega_n)$ at the angle $\theta = m\lambda/\lambda_p$ indicates that the diffraction orders will start to be resolvable when $(2\pi l/\lambda_p) > 1$. Thus as the pulse repetition rate increases and the number of pulses within the illumination interval increases (i.e., $2\pi l/\lambda_p \gg 1$), $(\sin\Omega_m/\Omega_m)(\sin\Omega_n/\Omega_n) \simeq 0$ for $m \neq n$, and the diffraction pattern becomes discrete, i.e.,

$$\bar{I}(\theta,t) = \bar{I}(\theta) = \sum_{m=-\infty}^{\infty} \left(\frac{\sin\Omega_m}{\Omega_m}\right)^2 I_m, \tag{16}$$

where

$$I_m = (\Psi_m^{\mathrm{Re}})^2 + (\Psi_m^{\mathrm{Im}})^2 = |\Psi_m|^2, \tag{17}$$

with I_m being the intensity in the mth diffraction order.

To illustrate the behavior of the diffracted light intensity as the ultrasonic pulse amplitude increases, Ψ_m can be factored into a series of approximate expressions based on successively higher Bessel function products, i.e., J_1; $J_1J_1J_1J_2$; $J_1J_1J_1J_2J_2J_1J_1J_1J_1J_2J_3$; etc.

A. First-order approximation

To determine how the diffraction order intensities initially develop we can examine Eq. (17) in the limit that the ν_n are small, i.e., products in Ψ_m of order $J_1(\nu_i)J_1(\nu_k)$ or higher vanish. Using this constraint and the relationship

$$m = r_1 + 2r_2 + \cdots + nr_n + \cdots, \tag{18}$$

used in the definition of Ψ_m, we find that for $m = 0$

$$I_0 = \left| \prod_{n=1}^{\infty} J_0(\nu_n) \right|^2 \tag{19}$$

and for $|m| > 0$,

$$I_{\pm m} = \left| J_{\pm 1}(\nu_m) e^{\pm i\phi_m} \prod_{n \neq m}^{\infty} J_0(\nu_n) \right|^2 . \tag{20}$$

Since $I_m = I_{-m}$, the diffraction pattern is symmetric about the central order. In the very small amplitude limit $I_0 \simeq 1.0$ and $I_{\pm m} \simeq \nu_m^2/4$. Thus the intensities in the individual diffraction orders provide a relative measure of the ultrasonic pulse's Fourier amplitude spectra.

B. Higher order approximations

As the pulse amplitude increases, the J_1J_1 and J_2 terms in Ψ_m begin to contribute and the intensity in the mth diffraction order ceases to be solely determined by $J_1(\nu_m)$ for $m > 0$. For the central diffraction order ($m = 0$) there are no additional terms due to the constraint imposed by Eq. (18). However, for the higher diffraction orders, i.e., $|m| > 0$, we find that the intensity is given by

$$\begin{aligned} I_{\pm m} = \Bigg| & J_{\pm 1}(\nu_m) e^{\pm i\phi_m} \prod_{n \neq m} J_0(\nu_n) + J_2(\nu_{m/2}) e^{\pm i2\phi_{m/2}} \prod_{k \neq m/2} J_0(\nu_k) \\ & + \sum_{\substack{n=1 \\ n<m-n}} \left(J_{\pm 1}(\nu_n) J_{\pm 1}(\nu_{m-n}) e^{\pm i(\phi_n + \phi_{m-n})} \prod_{k \neq n, m-n} J_0(\nu_k) \right) \\ & + \sum_n \left(J_{\mp 1}(\nu_n) J_{\pm 1}(\nu_{n+m}) e^{\pm i(\phi_{n+m} - \phi_n)} \prod_{k \neq n, n+m} J_0(\nu_k) \right) \Bigg|^2 , \end{aligned} \tag{21}$$

with the convention that all terms vanish with noninteger summation indices and when the indices of the ν_i are equal and that the summations and Π products are valid only over positive nonzero index values. The upper sign in the expression corresponds to the positive diffraction orders and the lower sign corresponds to the negative orders.

Since $J_{-n}(x) = (-1)^n J_n(x)$, the second-order terms in (21), $J_2(\nu_{m/2})$ and the two J_1J_1 product expressions, experience a 180° phase shift relative to $J_1(\nu_m)$ in going from $+m$ to $-m$. If these terms represent a net increase in amplitude when added to $J_1(\nu_m)$, there will be a corresponding net decrease when added to $J_{-1}(\nu_m)$. This causes the diffraction pattern to become asymmetric.

We can use Eq. (21) to illustrate the mechanisms involved in the growth of the farfield diffraction pattern. Based on Eq. (15), each diffraction order corresponds to a multiple of the pulse repetition rate ω_p. The first term in Eq. (21) represents the first Raman–Nath diffraction order for the mth Fourier component of the pulse. The second term represents the second Raman–Nath diffraction order of the $m/2$th pulse Fourier component. The J_1J_1 and J_1J_{-1} summations correspond to the mixing of the contributions of the pulse Fourier components, i.e., the sum and difference terms which result in $m\omega_p$. The resultant farfield diffraction pattern is the superposition of the Raman–Nath diffraction patterns of the pulse Fourier components and the mixing of these components as constrained by Eq. (18).

In the continuous wave limit all Fourier components of υ vanish except for the ν_n which corresponds to the pulse fundamental frequency. The resulting intensities $I_0 = J_0^2(\nu_n)$; $I_{\pm n} = J_1^2(\nu_n)$; and $I_{\pm 2n} = J_2^2(\nu_n)$ correspond to the zero, first, and second Raman–Nath diffraction orders.

The next highest approximation adds $J_1J_1J_1$, J_1J_2, and J_3 terms to the expression for the intensity. In the interest of brevity only the additions to Eq. (19) and Eq. (21) are shown with the phase and Π product expressions suppressed. In each case the additions are to the terms inside the absolute value signs. The central order is given by

$$\begin{aligned} I_0 = \Bigg| & \text{Eq. (19)} + \sum_{n=1} \{ J_{-2}(\nu_n) J_1(\nu_{2n}) + J_2(\nu_n) J_{-1}(\nu_{2n}) \} \\ & \times \sum_q \left\{ J_1(\nu_q) \left(\sum_{\substack{n=1 \\ n<q-n}} J_{-1}(\nu_n) J_{-1}(\nu_{q-n}) \right) + J_{-1}(\nu_q) \left(\sum_{\substack{n=1 \\ n<q-n}} J_1(\nu_n) J_1(\nu_{q-n}) \right) \right\} \Bigg|^2 , \end{aligned} \tag{22}$$

with the convention that all terms vanish with noninteger summation indices and when the indices of the ν_i are equal and that the summations are valid only over positive nonzero index values. The change for the higher orders ($|m| > 0$) is given by

$$\begin{aligned} I_{\pm m} = \Bigg| & \text{Eq. (21)} + \sum_{n=1} J_{\pm 2}(\nu_n) J_{\pm 1}(\nu_{m-2n}) + J_{\pm 3}(\nu_{m/3}) + \sum_{n=1} J_{\pm 2}(\nu_n) J_{\mp 1}(\nu_{2n-m}) + \sum_{n=1} J_{\mp 2}(\nu_n) J_{\pm 1}(\nu_{2n+m}) \\ & + \sum_{q=1} \left(J_{\pm 1}(\nu_q) \sum_{\substack{n=1 \\ n<q-m-n}} J_{\mp 1}(\nu_n) J_{\mp 1}(\nu_{q-m-n}) + J_{\mp 1}(\nu_q) \sum_{\substack{n=1 \\ n<q+m-n}} J_{\pm 1}(\nu_n) J_{\pm 1}(\nu_{q+m-n}) \right) \\ & + \sum_{\substack{q=1 \\ q+n<m-2q-n}} J_{\pm 1}(\nu_q) \sum_{n=1} J_{\pm 1}(\nu_{q+n}) J_{\pm 1}(\nu_{m-2q-n}) \Bigg|^2 \end{aligned} \tag{23}$$

using the same conventions as were imposed on Eq. (21). Since $J_{-n}(x)$ equals $(-1)^n J_n(x)$, the J_3, J_2J_1, and $J_1J_1J_1$ expressions maintain a constant phase relationship with $J_1(\nu_m)$ in going from $+m$ to $-m$. As a result, the associated increase or decrease in amplitude for the $+m$ and $-m$ orders is the same. In the continuous wave limit when all components of v vanish except ν_n the diffracted light intensities become $I_0 = J_0^2(\nu_n)$; $I_{\pm n} = J_1^2(\nu_n)$; $I_{\pm 2n} = J_2^2(\nu_n)$; and $I_{\pm 3n} = J_3^2(\nu_n)$. These correspond to the zero, first, second, and third Raman–Nath diffraction orders. Higher order terms will impact on the asymmetry in the diffraction pattern only if the sum of the Bessel function orders is even.

II. ANALYTIC RESULTS

This section provides examples of the diffracted light intensity distribution as a function of ν and the growth and decay of asymmetries within the diffraction pattern. For illustration the exponentially damped sinusoid given by Eq. (24) is used as the pulse time history.

$$v(t) = \nu e^{-\omega_0 t/2\pi k_1} \sin \omega_0 t \{h(t) - h(t - 2\pi k_2/\omega_0)\} e^{1/4k_1}, \tag{24}$$

where $h(t)$ is the Heaviside function, $\omega_0 = 2\pi f_0$ and, k_1 and k_2 determine the pulse decay and repetition rates. In this form a pulse with $k_1 = 10.0$ and $k_2 = 30.0$ has an e-folding time of $10\tau_0$ and a repetition rate of $30\tau_0$ where $\tau_0 = 1/f_0$. The Fourier amplitudes of v are $\nu_n = \nu a_n$ with $a_n = (c_n^2 + b_n^2)^{1/2}$ and c_n and b_n given by

$$c_n = \left(\frac{\epsilon_n - e^{-\Delta}\{\Delta \sin \epsilon_n + \epsilon_n \cos \epsilon_n\}}{\Delta^2 + \epsilon_n^2} + \frac{\gamma_n - e^{-\Delta}\{\Delta \sin \gamma_n + \gamma_n \cos \gamma_n\}}{\Delta^2 + \gamma_n^2} \right) e^{1/4k_1}, \tag{25}$$

$$b_n = \left(\frac{e^{-\Delta}\{\epsilon_n \sin \epsilon_n - \Delta \cos \epsilon_n\} + \Delta}{\Delta^2 + \epsilon_n^2} - \frac{e^{-\Delta}\{\gamma_n \sin \gamma_n - \Delta \cos \gamma_n\} + \Delta}{\Delta^2 + \gamma_n^2} \right) e^{1/4k_1}, \tag{26}$$

where $\Delta = k_2/k_1$, $\epsilon_n = 2\pi(k_2 - n)$, and $\gamma_n = 2\pi(k_2 + n)$. The phase ϕ_n is given by $\arccos(c_n/a_n)$ with the sign of ϕ_n determined by the quadrant within which c_n and b_n fall.

Figure 1 illustrates the amplitude and phase spectra of Eq. (24) when $k_1 = 10.0$ and $k_2 = 30.0$. For $f_0 = 3.0$ MHz the spectral components are spaced 100 kHz apart, the maximum amplitude occurs at 3.0 MHz, and the components above and below 3.0 MHz are approximately $\pi/2$ out of phase with a slight asymmetry in the amplitude spectra.

A. Farfield diffraction patterns

Using the spectra presented in Fig. 1 we can now examine the growth of the diffraction pattern as a function of the Raman–Nath parameter. This is shown in Fig. 2 based on Eqs. (22) and (23) for selected values of ν with an arbitrary intensity cutoff set at 0.1%, i.e., 1E-3, on the abscissa. In each part of Fig. 2, the diffraction orders are shown with the expected relative spatial separation.

Initially when $\nu = 0.5$ [Fig. 2(a)], the central order has

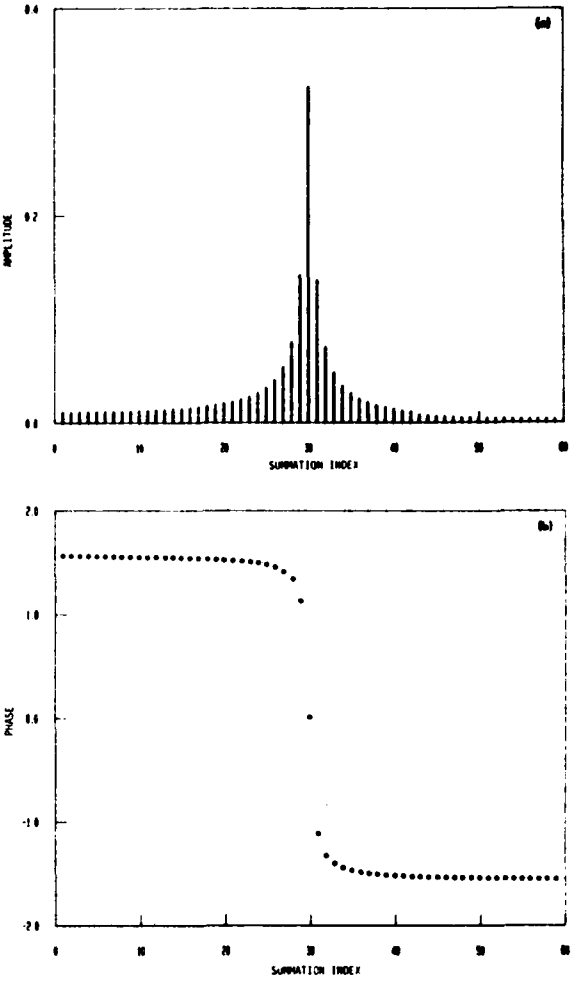

FIG. 1. (a) Pulse amplitude spectra for $\nu = 1.0$, $k_1 = 10.0$, and $k_2 = 30.0$. (b) Pulse phase spectra for $\nu = 1.0$, $k_1 = 10.0$, and $k_2 = 30.0$.

no satellite orders above the threshold and the pattern is almost symmetric. The positive and negative diffraction orders $I_{\pm 29}$ through $I_{\pm 31}$ locally follow the asymmetry which exists in the amplitude spectra [Fig. 1(a)]. As the pulse amplitude increases the second-order sum and difference terms previously discussed begin to introduce asymmetries into the pattern. At $\nu = 1.0$ [Fig. 2(b)] the local asymmetry in the satellite orders around I_{-30} has decreased at the same time that the asymmetry in the satellite orders around I_{+30} has started to increase. As the second-order terms continue to increase in magnitude the pattern becomes locally asymmetric around I_{-30} [Fig. 2(c)], the asymmetry between the positive and negative orders becomes more pronounced, and the satellite orders begin to appear locally about the central order. The asymmetry in $I_{\pm 1}$ through $I_{\pm 3}$ results from the $J_{-1}J_1$ terms in Eq. (21) being the same order of magnitude as $J_1(\nu_m)$. As the pulse amplitude continues to increase [Fig. 2(d)] the local asymmetry around the central order decreases as the asymmetry increases around $I_{\pm 30}$. At $\nu = 2.5$ [Fig. 2(e)], the number of satellite orders around the central order has increased at the same time that some of the satellite orders about $I_{\pm 30}$ have dropped below the intensity threshold.

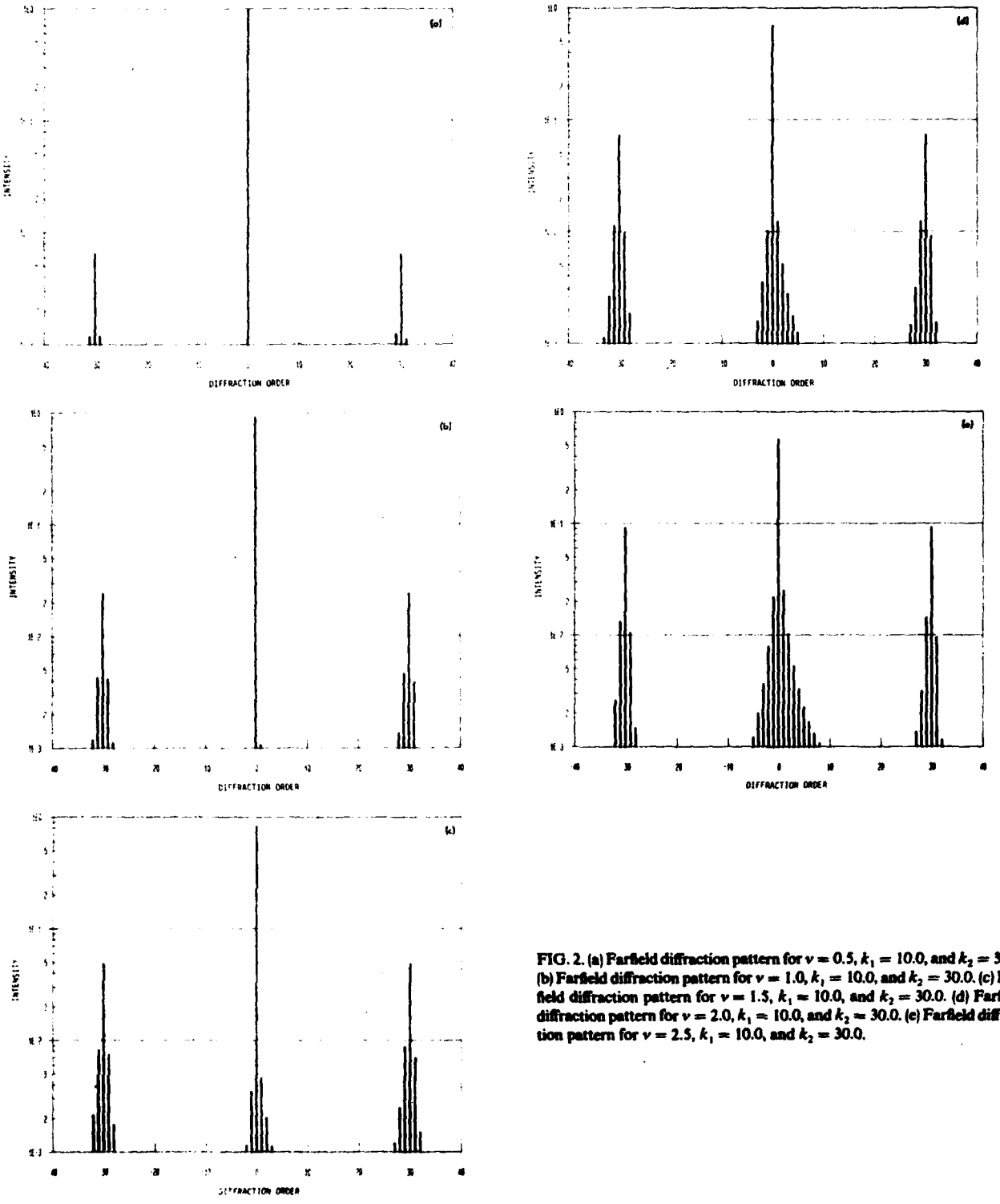

FIG. 2. (a) Farfield diffraction pattern for $\nu = 0.5$, $k_1 = 10.0$, and $k_2 = 30.0$. (b) Farfield diffraction pattern for $\nu = 1.0$, $k_1 = 10.0$, and $k_2 = 30.0$. (c) Farfield diffraction pattern for $\nu = 1.5$, $k_1 = 10.0$, and $k_2 = 30.0$. (d) Farfield diffraction pattern for $\nu = 2.0$, $k_1 = 10.0$, and $k_2 = 30.0$. (e) Farfield diffraction pattern for $\nu = 2.5$, $k_1 = 10.0$, and $k_2 = 30.0$.

B. Discussion of successive approximations

The contributions of the approximations in Eqs. (20)–(23) to the farfield diffraction pattern presented in Fig. 2 are illustrated in Fig. 3 as a function of ν. The first approximation Eq. (20) is given by the dotted line, the second approximation Eq. (21) by the dashed line, and the third approximation Eq. (23) by the solid line. For I_{30}, Eqs. (20) and (21) are approximately equal and Eq. (23) results in a small correction to the intensity. The apparent divergence of the approximations for I_{29} and I_{28} can be understood by examining the relative magnitudes of the individual contributions to the amplitude of the diffracted light intensity. For $\nu = 2.0$ and

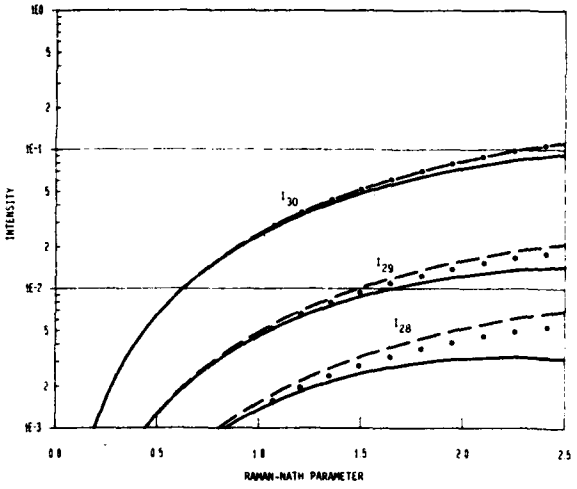

FIG. 3. Contribution of Eqs. (20)–(23) to I_{28} through I_{30} as a function of v for $k_1 = 10.0$ and $k_2 = 30.0$.

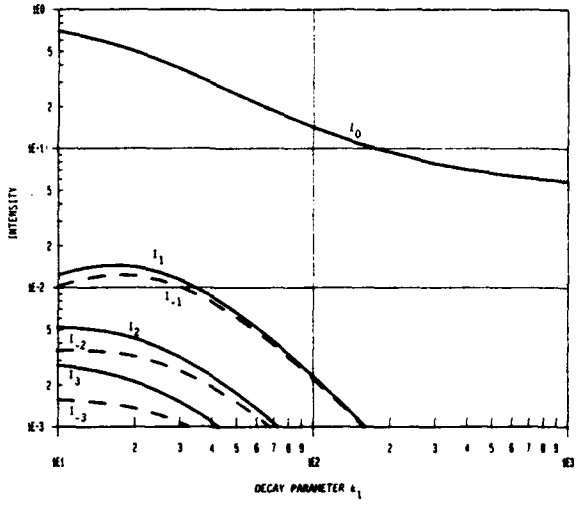

FIG. 5. I_{-3} through I_3 as a function of k_1 for $v = 2.0$ and $k_2 = 30.0$.

$m = 29$ the leading terms in the series approximations, Eqs. (20)–(23), excluding the phase and Π product expressions are $J_1(v_{29})$; $J_{-1}(v_1)J_1(v_{30})$; and $J_{-1}(v_{30})J_1(v_{28})J_1(v_{31})$. At the same time the validity of the approximation presented in Fig. 3 can be gauged by examining the leading terms of the next higher series approximations, $J_{-1}(v_2)J_{-1}(v_{30})J_1(v_{29})J_1(v_{31})$ and $J_{-1}(v_{27})J_1(v_{28})J_1(v_{29})J_1(v_{30})J_{-1}(v_{31})$. The associated magnitudes starting with $J_1(v_{29})$ are: 1.4×10^{-1}; 3.2×10^{-3}; 3.3×10^{-3}; 6.1×10^{-5}; and 2.5×10^{-5}, respectively.

For $v = 2.0$ and $m = 28$, the leading terms in the series expansion for the amplitude are: $J_1(v_{28})$; $J_{-1}(v_2)J_1(v_{30})$; $J_{-1}(v_{30})J_1(v_{27})J_1(v_{31})$; $J_{-1}(v_3)J_{-1}(v_{30})J_1(v_{29})J_1(v_{31})$; and $J_{-1}(v_{27})J_1(v_{28})J_1(v_{29})J_1(v_{30})J_{-1}(v_{32})$. The magnitudes, starting with $J_1(v_{28})$, are: 7.8×10^{-2}; 3.2×10^{-3}; 2.3×10^{-3}; 6.1×10^{-5}; and 9.7×10^{-6}, respectively. Based on the examination of I_{29} and I_{28} it is apparent that $J_1(v_m)$ for decreasing m drops in magnitude more rapidly than the leading terms for the higher approximations. Also, approximations beyond those presented in Eq. (23) will produce second-order corrections to the intensity over the range of interest. For $v > 1.0$, $m < 28$ or $m > 28$ become dominated by the product terms that correspond to the frequency associated with the order. For v above 3.0 higher order approximations ($J_1J_1J_1J_1$; $J_1J_1J_1J_1J_1$; etc.) will begin to produce first-order corrections to the intensity.

The development of asymmetries in the associated negative orders is shown in Fig. 4. As expected the contributions of the J_1J_1 and J_2 terms in Eq. (21) which add to I_{29} (Fig. 3) result in an equivalent reduction in I_{-29} (Fig. 4). Concurrently the higher order terms in Eq. (23) produce a reduction in both the positive and negative order intensities.

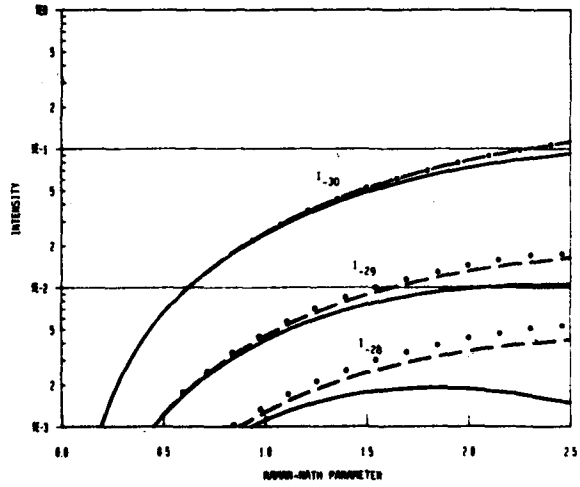

FIG. 4. Contribution of Eqs. (20)–(23) to I_{-28} through I_{-30} as a function of v for $k_1 = 10.0$ and $k_2 = 30.0$.

C. Continuous wave limit

In the limit that the pulse approaches a continuous wave the satellite orders vanish as shown in Fig. 5 for the central order ($v = 2.0$). As k_1 increases the pulse amplitude spectra approaches $v_m = 1.0$ for $m = 30$ and $v_m = 0.0$ for $m \neq 30$. This causes $J_1(v_m)$ to decrease more rapidly than the $J_{-1}(v_n)J_1(v_{m+n})$ terms locally around v_{30}. The pattern becomes symmetric locally about the central order and then vanishes as the central order intensity approaches $J_0^2(2)$.

III. EXPERIMENTAL RESULTS

To provide qualitative verification of the theory presented in Sec. I, an Arenberg pulser was used to excite a PZT transducer with a short pulse (3.0-MHz fundamental frequency). The resulting farfield diffraction pattern from a sequence of pulses is shown in Fig. 6 for a pulse duration of ~ 4 μs, a repetition rate of ~ 32 μs, and a Raman–Nath parameter of ~ 3.0. As predicted by the theory the splitting occurs in the central diffraction order and local asymmetry appears around $I_{\pm 48}$, the order associated with the pulse fundamental frequency. There is no discernable asymmetry for the satellite orders about the central order as would be expected for $v \sim 3.0$ due to the dominance of the J_1J_{-1} terms in Eq. (21).

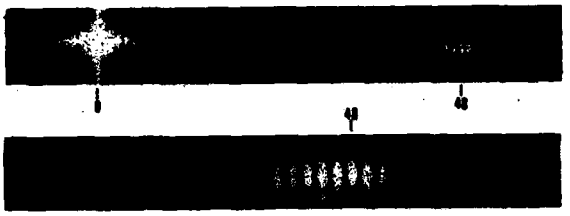

FIG. 6. Typical pulse diffraction pattern for 3.0-MHz pulses with 4 μs duration and 32 μs repetition rate. Top: photograph of orders up to $n = 60$, with $n = 48$ corresponding to location where the first order of a cw diffraction pattern would appear. Bottom: enlargement of orders around $n = 48$.

IV. SUMMARY

An analytic expression has been derived for the Raman–Nath diffraction by pulsed ultrasonic waves which can be applied to any general pulse shape amenable to spectral analysis. In general the resulting diffraction pattern is asymmetric around the central order with the degree of asymmetry dependent on the spectral composition of the pulse. A limited set of examples has been provided which demonstrates the degree of asymmetry for an exponential driving pulse and the convergence to the classic Raman–Nath results when the pulse approaches a continuous wave.

ACKNOWLEDGMENT

The research presented in this paper has been performed while one of the authors (T.H.N.) was a visiting member of the Georgetown University Physics Department. The other author (W.G.M.) acknowledges the support of the Office of Naval Research, Code 412.

[1]P. Debye and F. W. Sears, Proc. Natl. Acad. Sci. USA 18, 63 (1932).
[2]R. Lucas and P. Biquard, "Nouvelles propriétés optiques des solides et des liquides soumis á l'action des ondes ultrasonores," C. R. Acad. Sci. (Paris) 195, 121 (1932).
[3]C. V. Raman and N. S. N. Nath, "The diffraction of light by high frequency sound waves: Part I," Proc. Ind. Acad. Sci. II, 406–412 (1935).
[4]C. V. Raman and N. S. N. Nath, "The diffraction of light by sound waves of high frequency: Part II," Proc. Ind. Acad. Sci. II, 413–420 (1935).
[5]C. V. Raman and N. S. N. Nath, "The diffraction of light by high frequency sound waves: Part III," Proc. Ind. Acad. Sci. III, 75–84 (1936).
[6]J. S. Murty, "Theoretical investigations of the diffraction of light by superposed ultrasonic waves," J. Acoust. Soc. Am. 26, 970–974 (1954).
[7]K. L. Zankel and E. A. Hiedemann, "Diffraction of light by ultrasonic waves progressing with finite but moderate amplitudes in liquids," J. Acoust. Soc. Am. 31, 44–54 (1959).
[8]M. A. Breazeale and E. A. Hiedemann, "Investigation of progressive ultrasonic waves by light refraction," J. Acoust. Soc. Am. 30, 751–756 (1958).
[9]L. E. Hargrove, "Effects of ultrasonic waves on Gaussian light beams with diameter comparable to ultrasonic wavelength," J. Acoust. Soc. Am. 43, 847–851 (1968).
[10]R. N. Zitter, "Ultrasonic diffraction of light by short acoustic pulses," J. Acoust. Soc. Am. 43, 864–870 (1968).
[11]F. Calligaris, C. Cernigoi, and P. Ciuti, "Modulation effects of progressive ultrasonic fields on a light beam of variable width," Nuovo Cimento B 8, 157–166 (1972).
[12]F. Calligaris, P. Ciuti, and I. Gabrielli, "Extended theory of light modulation in thin-screen diffraction by ultrasound," J. Opt. Soc. Am. 63, 287–292 (1973).
[13]F. Calligaris, P. Ciuti, and I. Gabrielli, "Light modulation by ultrasound associated with an amplitude optical grating," Acustica 27, 307–313 (1972).
[14]E. Häusler, W. G. Mayer, and M. Schwartz, "Light diffraction by ultrasonic pulses," Acoust. Lett. 4, 180–184 (1981).

Theoretical prediction of a backscattering maximum at Rayleigh angle incidence for a smooth liquid–solid interface

Tran D. K. Ngoc
Code 5160, Naval Research Laboratory, Washington, DC 20375

Walter G. Mayer
Physics Department, Georgetown University, Washington, DC 20057

(Received 27 June 1983; accepted for publication 22 September 1983)

A numerical integration method for the description of acoustic bounded beams is used to calculate possible backscattering strength from a smooth liquid–solid interface. It is shown that the backscattering strength is maximum for Rayleigh angle incidence. The influence of beam shape and beamwidth on the backscattering strength near the maximum is demonstrated.

PACS numbers: 43.35.Pt, 68.25. + j, 43.20.Bi, 43.20.Fn

INTRODUCTION

Recently, an interesting phenomenon associated with the backscattering of a bounded acoustic beam from a smooth liquid–solid interface has been reported.[1] This phenomenon involves the existence of a relative maximum at the Rayleigh angle incidence when the backscattering strength is measured for various incident angles. First, de Billy, Adler, and Quentin[1] reported on this maximum of backscattering strength for a water–stainless steel and a water–copper interface. The same authors later considered a more general scattering geometry and observed[2] a relative maximum in the scattering strength at both backward-scattered and forward-scattered Rayleigh angles for a general incident angle. Indeed, these observations, described as conical reflection, have been qualitatively reported[3] earlier by Diachok and Mayer for the specific case of Rayleigh angle incidence.

These experimental results have prompted several theoretical investigations attempting to explain these phenomena. Within the context of spectral representation of acoustic bounded beams, Norris[4] extended the Bertoni and Tamir analytical procedure,[5] developed for forward reflection, to the backscattering case. In light of the fact that surface roughness should play a significant role in backscattering measurements, de Billy and Quentin[6] employed the potential method as described by Welton[7] to evaluate the acoustic field of a bounded beam scattered from a rough liquid–solid interface. Comparing their theoretical results with backscattering measurements on samples with rough interfaces, de Billy and Quentin showed good agreement for incident angles of 40° or less except that their theory did not account for the relative maximum observed near the Rayleigh critical angle.

The above theoretical efforts[4,6] appear to confirm the belief that the relative maximum of backscattering strength at Rayleigh angle incidence must be associated with the boundedness of the acoustic source as well as the resonant surface propagation mode corresponding to the Rayleigh critical angle. Under this motivation the present study intends to investigate this backscattering phenomenon of a smooth liquid–solid interface, using an exact numerical integration algorithm to evaluate the scattered acoustic field described by the spectral representation. This numerical algorithm was initially developed by Ngoc and Mayer[8] to describe acoustic bounded beams reflected from or transmitted through layered media. As will be shown in the following calculation results, this theoretical analysis is able to describe the general features of backscattering strength as a function of incident angle, including the relative maximum at the Rayleigh critical angle.

I. THEORY AND COMPUTATIONAL RESULTS

Following the formulation developed by Ngoc and Mayer,[8] the spectral representation is again invoked to describe the scattered field of an acoustic bounded beam of frequency ω incident onto a smooth liquid–solid interface at an incident angle θ_i,

$$U(x,z) = (2\pi)^{-1}\int_{-k}^{k} R(k_x)\, V(k_x) \times \exp[i(xk_x + zk_z)]\, dk_x. \quad (1)$$

The symbols used in above equation are defined as follows: $U(x,z)$ is the acoustic scattered field in the (x,z) plane assuming uniformity in the y dimension; k is the wave vector in the liquid; k_x and k_z are the x and z components of the k vector related by $k_z = (k^2 - k_x^2)^{1/2}$. The quantity $R(k_x)$ denotes the plane-wave reflection coefficient at a liquid–solid interface (e.g., see Ref. 8) and $V(k_x)$ is the Fourier transform of the incident acoustic beam given at the interface, describing the complex amplitude of the constituent plane waves that form the incident beam.

In calculating the scattered sound field the integral of Eq. (1) is interpreted as describing the scattered field represented by a superposition of plane waves having the complex amplitude $R(k_x)V(k_x)$. Integrating from $-k$ to k implies that contributions to the scattered field can come from plane waves reflected in all directions from this interface. To be compatible with most experimental arrangements, transducers of finite size for both acoustic source and detector will be taken into account in the present study. In addition, one would also like to be able to account for the specific response pattern of the detector in use. The scattering geometry adopted in the following computations is illustrated in Fig. 1. The source and detecting transducers, both having a width

 0001-4966/84/010168-03$00.80

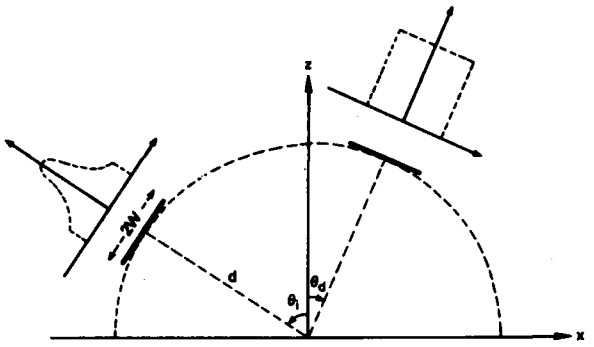

FIG. 1. Schematic description of the scattering geometry under consideration.

of $2w$, are rotated on semicircular paths of radius d. The incident and detecting angles are defined as θ_i and θ_d, respectively. The positive direction of these angles is indicated by the underlying arrows and therefore detection of the backscattered sound would assume a negative value for θ_d. For the backscattering geometry, $\theta_d = -\theta_i$.

In the backscattering calculations to be presented, the incident beam profile is taken to be a finite Gaussian one and the detecting transducer is assumed to have a flat response. The calculations are carried out according to the following procedure:

(a) For a given θ_i, the incident beam profile is first projected onto the $z = 0$ interface;

(b) The projected incident profile is then Fourier transformed to yield $V(k_x)$;

(c) Interaction of individual plane waves of complex amplitude $V(k_x)$ with the interface is described by the product $R(k_x)V(k_x)$, which is now entered into the integrand of Eq. (1);

(d) The scattered acoustic field at spatial position (x,z) can now be evaluated by an exact numerical integration of Eq. (1) across the surface of the detecting transducer, which can be represented by

$$z = \tan\theta_d(d - x)$$

for

$$d\sin\theta_d - w\cos\theta_d < x < d\sin\theta_d + w\cos\theta_d; \qquad (2)$$

(e) The backscattering strength for a given $\theta_d = -\theta_i$ is finally determined from the scattered field calculated across the detecting surface in the preceding step by averaging them according to the selected response of the detector.

Figure 2 presents the first set of computational results showing backscattering strength as a function of incident angle for three values of beamwidth, $2w = 5$, 10, and 20 mm, with an acoustic source of 2 MHz. These computations are done for a water–stainless steel interface with the radial distance d being 50 mm. The backscattering strength curves shown in Fig. 2 exhibit a steady decrease as the incident angle becomes larger, with a distinct relative maximum positioned approximately at the Rayleigh critical angle which is calculated to be 30.65° in this case. Near the relative maximum one observes that the maximum peak increases with beamwidth and the slope of the maximum is broadened at the base for smaller beamwidths.

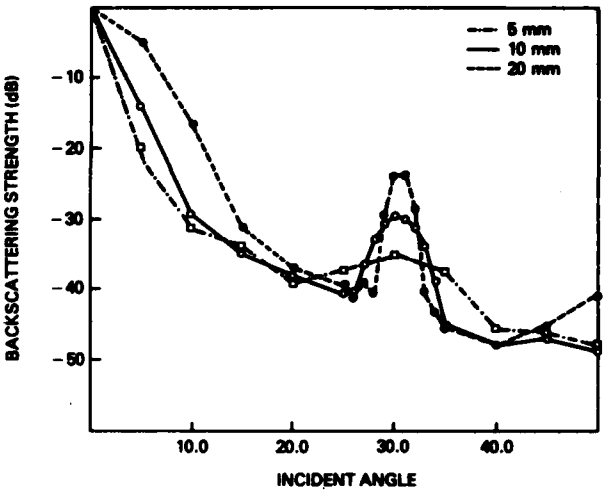

FIG. 2. Variation of backscattering strength with beamwidth for a finite Gaussian beam of 2 MHz incident on a water–stainless steel interface.

Next, the beamwidth is kept constant at the value of 10 mm but the shape of the incident Gaussian profile is varied. This is achieved by introducing a parameter α in the expression describing a Gaussian profile,

$$U_{\text{inc}}(x) = \exp - [(x/\alpha w)^2]. \qquad (3)$$

Setting $\alpha = 1$ corresponds to the incident profile used in the previous set of calculations. In the present set of calculations, the incident beam generated by setting $\alpha = 0.5$ has a narrower profile while $\alpha = 2.0$ results in a broader profile. These incident profiles are illustrated in Fig. 3.

Again, the above computational procedure is applied to calculate the backscattering strength versus the incident angle for the three incident profiles shown in Fig. 3. The results are presented in Fig. 4 where the steady decrease, interrupted by a relative maximum near the Rayleigh angle, is observed for all of these profiles. The most noticeable difference among them is that the relative maximum is consider-

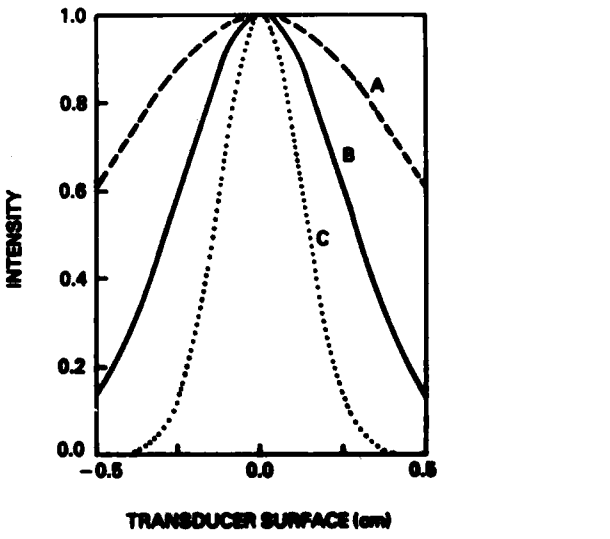

FIG. 3. Three Gaussian incident profiles of different shapes used in computations of backscattering strength.

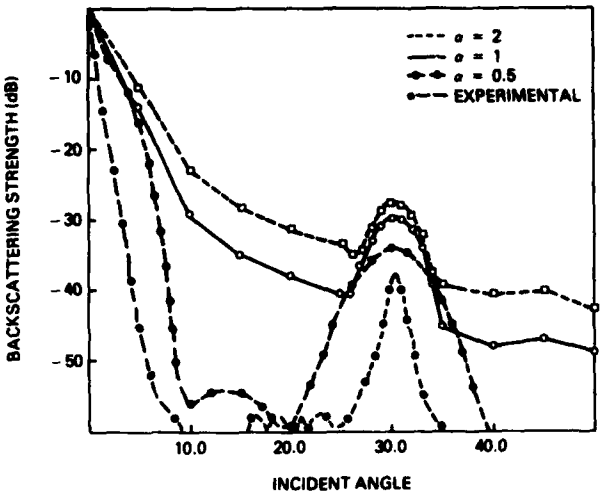

FIG. 4. Variation of backscattering strength due to changes in shape of the incident profile. The experimental curve is redrawn from Ref. 1 for the case of a Gaussian beam of 4.5 MHz and 12-mm beamwidth, incident on a water–stainless steel interface with other parameters not specified.

ably more pronounced when the incident beam profile becomes narrower. A typical experimentally obtained curve of backscattering strength is redrawn from Ref. 1 and is included in Fig. 4 for comparison.

II. CONCLUSION

The above computations establish that a theoretical description based on spectral analysis successfully predicts a relative backscattering maximum at the Rayleigh critical angle and other general features of the backscattered sound field observed by recent experimental measurements. A preliminary application of this theoretical approach has identified two key parameters that would affect the backscattering strength as a function of the incident angle. These two parameters are beamwidth and profile shape of the incident beam. It is expected from this formulation that other parameters including response pattern of the detector and distance of source and/or detector from the interface would also strongly influence the backscattering strength.

ACKNOWLEDGMENTS

This work was supported by the Office of Naval Research, Code 412. One of the authors (T.D.K.N.) acknowledges partial support by the Naval Electronics System Command, Code 612.

[1] M. de Billy, L. Adler, and G. J. Quentin, "Parameters affecting backscattered ultrasonic leaky Rayleigh waves from liquid–solid interfaces," J. Acoust. Soc. Am. 72, 1018 (1982).
[2] L. Adler, M. de Billy, and G. J. Quentin, "Excitation of ultrasonic Rayleigh waves at liquid–solid interface for general angle incidence," J. Appl. Phys. 53, 8756 (1982).
[3] O. I. Diachok and W. G. Mayer, "Conical reflection of ultrasound from a liquid–solid interface," J. Acoust. Soc. Am. 47, 155 (1970).
[4] A. N. Norris, "Back reflection of ultrasonic waves from a liquid–solid interface," J. Acoust. Soc. Am. 73, 427 (1983).
[5] H. L. Bertoni and T. Tamir, "Unified theory of Rayleigh-angle phenomena for acoustic beams at liquid–solid interface," Appl. Phys. 2, 157 (1973).
[6] M. de Billy and G. Quentin, "Backscattering of acoustic waves by randomly rough surfaces of elastic solids immersed in water," J. Acoust. Soc. Am. 72, 591 (1982).
[7] P. J. Welton, "The potential-method formulation of acoustic-wave scattering by rough surfaces," J. Acoust. Soc. Am. 54, 66 (1973).
[8] T. D. K. Ngoc and W. G. Mayer, "A general description of ultrasonic nonspecular reflection and transmission effects for layered media," IEEE Trans. Sonics Ultrason. SU-27, 229 (1980).

NONSPECULAR EFFECTS FOR A FINITE INCIDENT BEAM MODELED BY AN EVEN-ORDERED POLYNOMIAL

Tran D. K. Ngoc and Walter G. Mayer

Reprinted from IEEE Transactions on Sonics and Ultrasonics, Vol. SU-30, No. 4, July 1983

Correspondence

Nonspecular Effects for a Finite Incident Beam Modeled by an Even-Ordered Polynomial

TRAN D. K. NGOC AND WALTER G. MAYER

Abstract -The reflection of non-Gaussian ultrasonic beams, expressed in terms of *n*th-ordered polynomials, is discussed and it is shown that at critical longitudinal and Rayleigh angles of incidence deviations from the Gaussian profile case occur, varying with the polynomial representation chosen. Examples are given for water-Plexiglas and water-stainless steel flat interfaces.

INTRODUCTION

Nonspecular reflection and transmission effects of a finite sound beam have been investigated [1]-[7] for various types of layered media. Bertoni and Tamir's analysis [1] described these effects at the Rayleigh critical angle for a liquid-solid interface. Pitts *et al.* [2] extended Bertoni and Tamir's approach to another structure in which a solid plate is immersed in a liquid medium. This approach again was able to describe nonspecular effects at the critical plate-mode angles associated with Lamb waves of the solid plate. The problem was generalized to incorporate sound attenuation in the media and was solved numerically by Ngoc and Mayer [3]-[6]. This led to a description of nonspecular reflection and transmission effects at all incident angles where these effects may occur. The numerical approach enabled the discovery of nonspecular effects at the longitudinal critical angle [3] of the liquid-solid structure and at the between-mode angles [5] of the liquid-solid-liquid structure in addition to those taking place at the Rayleigh angle and the critical plate-mode angles of the respective structures. It was also able to describe the variation of nonspecular features as the incident beam was steered away from the critical angles.

The results of these studies provided an adequate understanding of the physical processes that underlie the nonspecular effects taking place upon reflection from or transmission through a flat interface. However, a major deficiency of the above theoretical models that limits the application of these effects to practical problems rests with the fact that these analyses are all based on the assumption of an incident beam having a Gaussian intensity distribution.

In most practical situations where one finds a sound beam incident at an interface, the incident beam profile would invariably be non-Gaussian. This is due to the fact that all acoustic beams traveling in any kind of medium must be subjected to several mechanisms that will distort the beam patterns [8], [9]. Such mechanisms include, for example, nonlinear interaction, absorption, geometrical diffraction, and dispersion of the medium itself. These mechanisms would sometimes change the beam pattern produced by the transducer by enhancing or reducing the side lobes. It is therefore quite desirable to be able to understand how an incident beam with sidelobes be-

Manuscript received November 8, 1982; revised April 26, 1983. This work was supported by the Office of Naval Research under code 412.

The authors are with the Physics Department, Georgetown University, Washington, DC 20057.

0018-9537/83/0700-0276$01.00

haves after interacting with an interface. In addition, one would also like to know if sidelobes are generated as part of nonspecular reflection or transmission of a non-Gaussian incident beam. As a result one can distinguish the changes in beam profile due to the nonspecular effects from those produced by the above-mentioned mechanisms associated with the medium.

In general, the current theoretical models describing nonspecular effects would become more useful if they allowed for treatment of incident beams of an arbitrary intensity distribution. In this paper, the numerical approach developed for Gaussian incident beam will be modified to investigate the nonspecular effects for incident beams having an nth-order polynomial intensity distribution. The choice of the polynomial distribution was motivated by the consideration that polynomial distributions can approximate very well many transducers in current use; furthermore, they can be adapted to be used as basic components to construct an arbitrary intensity distribution. In the following, modifications to the theoretical framework will be illustrated and sample nonspecular reflected beam profiles computed from the modified theory will be presented.

Theoretical Formulation

Consider a finite beam bounded in the (x, z) plane and uniform in the y-dimension, of angular frequency $\omega = 2\pi f$ and beam width $2w$. A spectral representation of such a bounded beam treats it as a superposition of an infinite number of plane waves having the same frequency but different amplitude and incident at slightly different angles about a central direction indicated by θ_i. Extending the principle of spectral representation to a reflected or transmitted bounded beam one can describe the reflected or transmitted field distribution by

$$U(x, z) = (2\pi)^{-1} \int_{k_i - \pi/w_0}^{k_i + \pi/w_0} P(k_x)\, V(k_x) \cdot \exp\left[i(xk_x + zk_z)\right] dk_x, \tag{1}$$

where $P(k_x)$ is the plane wave reflection or transmission coefficient for the layered structure under consideration. As before [5], $V(k_x)$ is the Fourier transform of the incident field and $w_0 = w/\cos\theta_i$ and $k_i = k \sin\theta_i$.

The present study investigates an incident beam described by an nth-order polynomial and compares the computational results with those for a Gaussian incident beam. Since most sound beams in practice are symmetric only the even orders of polynomials are considered. The specific form of the polynomials used to model the incident beam in this study are taken to be

$$U_{2n}(x, 0) = \begin{cases} A_{2n}\left[1 - (x/w_0)^2\right]^n, & -w_0 \leq x \leq w_0; \\ 0, & \text{elsewhere}, \end{cases} \tag{2}$$

where A_{2n} is the normalization constant. In order that reflected beam profiles calculated for a polynomial-type incident beam can be compared to those for Gaussian beams, A_{2n} will be normalized according to

$$A_{2n}^2 \int_{-w_0}^{w_0} \left[1 - (x/w_0)^2\right]^{2n} dx = \int_{-w_0}^{w_0} |U_g|^2\, dx, \tag{3}$$

where $U_g(x, 0)$ is the Gaussian incident distribution given by

$$U_g(x, 0) = \exp\left[-(x/w_0)^2 + ixk_i\right]. \tag{4}$$

Evaluation of the right-hand side of (3) yields

$$\int_{-w_0}^{w_0} |U_g|^2\, dx = (\pi/2)^{1/2}\, w_0\, \mathrm{erf}\,(\sqrt{2}), \tag{5}$$

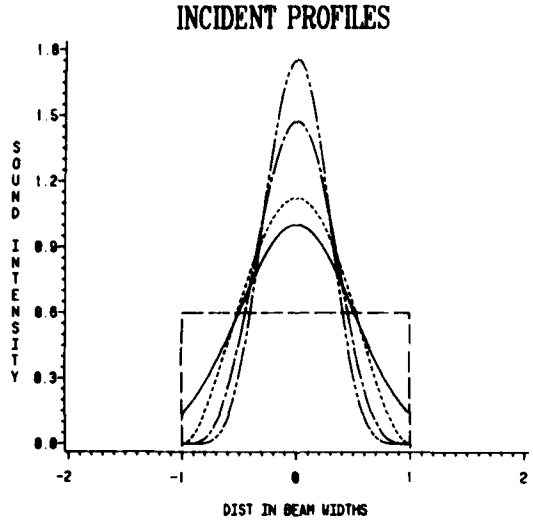

Fig. 1. Profile of incident beam represented by zero-ordered polynomial [step function] (long dashes); 2nd-ordered polynomial (short dashes); 4th-ordered polynomial (dash-dot); 6th-ordered polynomial (dash-double dot); and a Gaussian distribution (solid line).

where the function $\mathrm{erf}(x)$ is defined by

$$\mathrm{erf}(x) = 2/(\pi)^{1/2} \int_0^x \exp\left[-t^2\right] dt. \tag{6}$$

Combination of (3) and (5) gives the normalization constants A_{2n} up to the sixth order as

$$\begin{aligned} A_0 &= 0.7734, \\ A_2 &= 1.0590, \\ A_4 &= 1.2132, \\ A_6 &= 1.3243. \end{aligned} \tag{7}$$

The normalized intensity profiles of the even-ordered polynomial incident beams and the Gaussian intensity profile are presented in Fig. 1 for comparison. It is noted that the analysis of the general even-ordered polynomial beams also covers the special case of a piston source, where $n = 0$.

In order to evaluate the reflected or transmitted sound field from (1), one needs to determine $V(k_x)$ from the polynomial incident profile given by (2). This results in

$$\begin{aligned} V_{2n}(\alpha) = {} & 2w_0 \sum_{m=0}^{n} a_{nm} \left[\frac{\sin\alpha}{\alpha} \sum_{p=0}^{m} \frac{b_{mp}}{\alpha^{2p}} + \frac{\cos\alpha}{\alpha} \sum_{q=1}^{m} \frac{c_{mq}}{\alpha^{2q-1}}\right], \quad \text{for } \alpha \neq 0; \\ = {} & 2w_0 \sum_{m=0}^{n} a_{nm} \left[\sum_{p=0}^{m} b_{mp} \frac{(-1)^p}{(2p+1)!} + \sum_{q=1}^{m} c_{mq} \frac{(-1)^q}{(2q)!}\right], \quad \text{for } \alpha = 0. \end{aligned} \tag{8}$$

where

$$\begin{aligned} \alpha &= (k_i - k_x)\, w_0, \\ a_{nm} &= [(-1)^n n!(2m)!]/[m!(n-m)!], \quad \text{for } m = 0, 1, 2, \cdots, n, \\ b_{mp} &= (-1)^p/(2m-2p)!, \quad \text{for } p = 0, 1, 2, \cdots, m, \\ c_{mp} &= [(-1)^{q+1}]/[(2m-2q+1)!], \quad \text{for } q = 0, 1, 2, \cdots, m. \end{aligned}$$

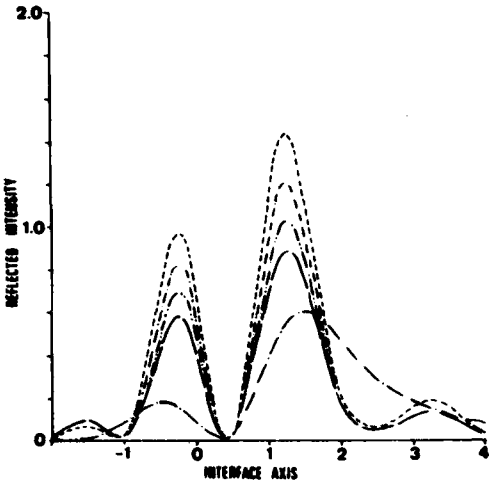

Fig. 2. Rayleigh angle reflection from a water–stainless steel flat interface for a Gaussian incident beam (long dash-dot); zero-ordered polynomial (short dashes); 2nd-ordered polynomial (short dashes-dots); 4th-ordered polynomial (short dashes-double dots); 6th-ordered polynomial (long dashes).

Evaluation of the integral in (1) to determine the reflected or transmitted sound field is now possible since $V(k_x)$ has been determined and the plane wave reflection or transmission coefficient $P(k_x)$ for several layered media is well established [5].

Computational Results

The nonspecular effects for an incident beam having an even-ordered polynomial profile are illustrated here for the simple case of a bounded beam reflected from a liquid–solid interface. Calculations are performed for the Rayleigh critical angle of a water–stainless steel interface and for the longitudinal critical angle of a water–Plexiglas structure.

In Fig. 2, the nonspecularly reflected beam profile at the Rayleigh angle is presented for both types of incident profiles. In the well-known case of a Gaussian profile, the reflected profile shows the familiar two peaks with a trailing field on both sides of the beam. However, reflected profiles associated with the even-ordered polynomial incident beam all exhibit distinct sidelobes in place of the trailing field. Among profiles of different orders, the profiles of lower orders have a higher reflection intensity level as measured by the magnitude of the two principal peaks. In general, one observes that the polynomial description of the incident beam does not change the fundamental nonspecular features other than the appearance of the sidelobes.

For the water–Plexiglas interface, nonspecular effects are investigated for the longitudinal critical angle. Results of an earlier study [3] for a Gaussian incident beam only showed the nonspecular feature of a lateral displacement. For the case of polynomial incident beams the nonspecularly reflected beams for all orders considered are again characterized by a lateral displacement of approximately the same magnitude. Sidelobes, although discernable but very small, are also present on both sides of the main peak. These results are illustrated in Fig. 3. The appearance of sidelobes in both sets of calculations is definitely associated with the choice of an nth-ordered polynomial for the incident beam distribution. For such a distribution, decomposition of the incident beam into plane

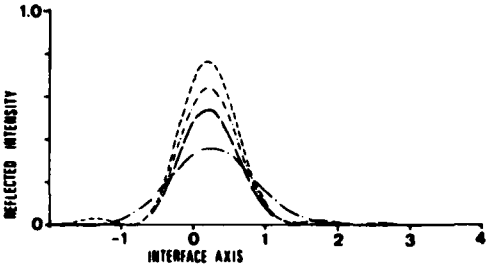

Fig. 3. Critical longitudinal angle reflection from a water–Plexiglas flat interface for a Gaussian incident beam (long dashes-dots); zero-ordered polynomial (short dashes); 2nd-ordered polynomial (short dashes-dots); 4th-ordered polynomial (long dashes).

waves as represented by its Fourier transform $V_{2n}(\alpha)$ shows contributions from plane waves deviating considerably from the central direction are quite significant and vary according to $\sin\alpha/\alpha$ or $\cos\alpha/\alpha$. As a result, the trailing field which always exists in the case of a Gaussian incident profile is no longer present and sidelobes are introduced into the reflected profiles.

Conclusion

The description of a finite incident beam by an even-ordered polynomial has been shown to lead to a new nonspecular feature in the reflected beam profile. The computational results predict that upon reflection at the critical angles associated with layered media, sidelobes will appear in the reflected profile if the incident beam has a polynomial distribution instead of a Gaussian one. The present study can form a basis for investigations of nonspecular reflection or transmission of an incident beam having an arbitrary intensity distribution which can be modeled through polynomial fitting.

References

[1] H. L. Bertoni and T. Tamir, "Unified theory of Rayleigh-angle phenomena for acoustic beams at liquid–solid interface," *Appl. Phys.*, vol. 2, pp. 157–172, 1973.

[2] L. E. Pitts, T. J. Plona, and W. G. Mayer, "Theory of nonspecular reflection effects for an ultrasonic beam incident on a solid plate in a liquid," *IEEE Trans. Sonics Ultrason.*, vol. SU-24, pp. 101–109, 1977.

[3] T.D.K. Ngoc and W. G. Mayer, "Ultrasonic nonspecular reflectivity near longitudinal critical angle," *J. Appl. Phys.*, vol. 50, pp. 7948–7951, 1979.

[4] —, "Numerical integration method for reflected beam profiles near Rayleigh angle," *J. Acoust. Soc. Amer.*, vol. 67, pp. 1149–1152, 1980.

[5] —, "A general description of ultrasonic nonspecular reflection and transmission effects for layered media," *IEEE Trans. Sonics Ultrason.*, vol. SU-27, pp. 229–236, 1980.

[6] —, "Influence of plate mode structure and Gaussian beam profile characteristics on ultrasonic reflection and transmission," *IEEE Trans. Sonics Ultrason.*, vol. SU-29, pp. 112–114, 1982.

[7] J. M. Claeys and O. Leroy, "Reflection and transmission of bounded sound beams on half-spaces and through plates," *J. Acoust. Soc. Amer.*, vol. 72, pp. 585–590, 1982.

[8] D. D. McLennan, T.D.K. Ngoc, and W. G. Mayer, "Measurements of harmonic profiles of a bounded ultrasonic beam in a liquid medium," in *Ultrasonics*, vol. 21, pp. 103–106, 1983.

[9] M. A. Breazeale, L. Adler, and G. W. Scott, "Interaction of ultrasonic waves incident at the Rayleigh angle onto the liquid–solid interface," *J. Appl. Phys.*, vol. 48, pp. 530–537, 1977.


DA
FILM